Modeling and experimental evaluation of membrane distillation aimed at urine treatment for direct potable reuse in space stations

Desalination 572 (2024) 117119

Contents lists available at ScienceDirect

Desalination

journal homepage: www.elsevier.com/locate/desal

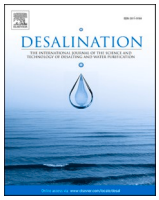

Modeling and experimental evaluation of membrane distillation aimed at urine treatment for direct potable reuse in space stations

Ali Naeimi Tabasian [a,b], Francesco Ricceri [a,b], Matteo Morciano [b,c], Giorgio Boscheri [d], Rachele Perelli [d], Matteo Fasano [b,c,*], Alberto Tiraferri [a,b,**]

[a] Department of Environment, Land and Infrastructure Engineering, Politecnico di Torino, Corso Duca degli Abruzzi 24, 10129 Turin, Italy
[b] Clean Water Center, Politecnico di Torino, Corso Duca degli Abruzzi 24, 10129 Turin, Italy
[c] Department of Energy, Politecnico di Torino, Corso Duca degli Abruzzi 24, 10129 Turin, Italy
[d] Domain Exploration and Science Italy (DESI), Thales Alenia Space Italia, Strada Antica di Collegno 253, 10149 Turin, Italy

HIGHLIGHTS

- A transient 2-D model was developed for DCMD treating wastewater for potable use.
- The modeled water flux and the ammonia passage were confirmed by experiments.
- The feed pH and operative conditions effects were analyzed.
- 8 L of urine can be daily treated at 40 °C with 0.1 m^2 membrane area.
- The average ammonia flux was limited to 0.03 $gm^{-2}h^{-1}$, easing post-treatment.

ARTICLE INFO

Keywords:
Membrane distillation
Space exploration
2D transient model
Urine recovery
Water reuse

ABSTRACT

Improving wastewater reuse systems represents a game changer for the economy of space exploration activities. The goal of this research is to evaluate direct contact membrane distillation for the treatment of urine aimed at direct potable reuse in space stations. A transient, 2-D model able to predict the membrane distillation system behavior under different operating conditions is developed. The model is validated by experimental tests conducted with a synthetic urine-like feed solution, considering both productivity and final water quality. The water flux and quality analyses imply high rejection of soluble salts and organics. However, direct water reuse may be compromised by the ammonia passage. A sensitivity analysis is thus performed to investigate the effects of feed pH, temperature, and cross-flow velocity on water flux and ammonia passage. The system shows the capability of treating 8 L of urine up to 90–95 % recovery rate, during 10 h of daily operation at 40 °C feed and 20 °C distillate inlet temperatures. This amount is sufficient to satisfy four crew members while meeting high system compactness. Concurrently, the ammonia passage may be limited by lowering the feed pH, thus easing the post-treatment steps necessary for safe direct reuse.

1. Introduction

Space economy is defined by the OECD Space Forum as "the full range of activities and the use of resources that create value and benefits to human beings in the course of exploring, understanding, managing and utilizing space" [1]. The term includes both current and upcoming activities, such as satellite communications, navigation, Earth observation, space transportation, space exploration, on-orbit manufacturing, space tourism, and resource extraction [1]. All such activities necessitate more sustainable space stations with advanced technologies, as well as the reduction of shipment and operational costs. The effective and economically advantageous recovery of life supporting resources, chiefly, water, food, and oxygen, may represent a game changer for space exploration activities [2,3]. Moreover, while space transportation has progressed considerably over the years, shipment

* Correspondence to: M. Fasano, Clean Water Center, Politecnico di Torino, Corso Duca degli Abruzzi 24, 10129 Turin, Italy.
** Correspondence to: A. Tiraferri, Department of Environment, Land and Infrastructure Engineering, Politecnico di Torino, Corso Duca degli Abruzzi 24, 10129 Turin, Italy.
E-mail addresses: matteo.fasano@polito.it (M. Fasano), alberto.tiraferri@polito.it (A. Tiraferri).

https://doi.org/10.1016/j.desal.2023.117119
Received 20 September 2023; Received in revised form 2 November 2023; Accepted 3 November 2023
Available online 10 November 2023

Nomenclature

a	Activity
B	Membrane permeability coefficient, $kg\,m^{-2}Pa^{-1}s^{-1}$
C	Concentration, $g\,L^{-1}$
C_p	Specific heat capacity, $J\,kg^{-1}K^{-1}$
d	Membrane thickness, m
d_p	Membrane average pore size, m
D	Diffusion coefficient, m^2s^{-1}
J	Transmembrane flux, $kg\,m^{-2}s^{-1}$
k	Thermal conductivity, $W\,m^{-1}K^{-1}$
k_f	Fluid thermal conductivity, $W\,m^{-1}K^{-1}$
k_B	Boltzmann constant, $J\,K^{-1}$
Kn	Knudsen number
m	Molality, $mol\,kg^{-1}$
M	Molecular weight, $kg\,mol^{-1}$
n_1°	Water molality, $mol\,kg^{-1}$
P	Pressure, Pa
Pe	Peclet Number
r	Membrane average pore radius, m
R	Gas constant, $J\,mol^{-1}K^{-1}$
S	Salinity, $g\,L^{-1}$
t	Time, s
T	Temperature, K
u	Cross flow velocity, $m\,s^{-1}$
V	Velocity vector, $m\,s^{-1}$
V_{tank}	Tank volume, L
W	Module width, m
x	x direction
z	z direction

Greek letters

ε	Membrane porosity
λ	Latent heat of evaporation, $J\,kg^{-1}$
λ_w	Mean free path of molecules, m
υ	Stochiometric coefficient of component
ρ_f	Fluid density, $g\,L^{-1}$
τ	Membrane tortuosity factor

Subscripts

a	Air
d	Distillate
f	Feed
i	Component index
in	Inlet
m	Membrane
x	x direction
z	z direction

costs are still high, usually above $10,000 per kg. Therefore, minimizing weight and improving the design of systems used for resource recovery would also result in reduced shipment costs, and these goals should be achieved within the constraints of safe operations. In turn, the same resource extraction and reuse technologies developed for space exploration may then be implemented on Earth, with a lasting impact for life on this Planet.

Among resource recovery technologies for space applications, those related to direct potable water reuse are of foremost importance. Urine is one of the main sources of recovered water in space stations, together with hygiene wastewater and with the crews' vapor from perspiration and respiration [4]. Systems for water recovery from such waste resources have been investigated over the years, especially by space agencies, such as NASA and ESA, with the aim to meet biological needs and to improve human waste management strategies [5]. The ideal water recovery system for space stations should be able to provide the highest recovery rate, the highest rejection of harmful contaminants, the highest compactness, the lowest weight, and the lowest energy and exergy requirements [6]. The current water recovery system utilized in the International Space Station (ISS) is schematically shown in Fig. 1. According to recent literature, the water recovery system consists of two major sections, namely, a urine processor assembly (UPA) and a water

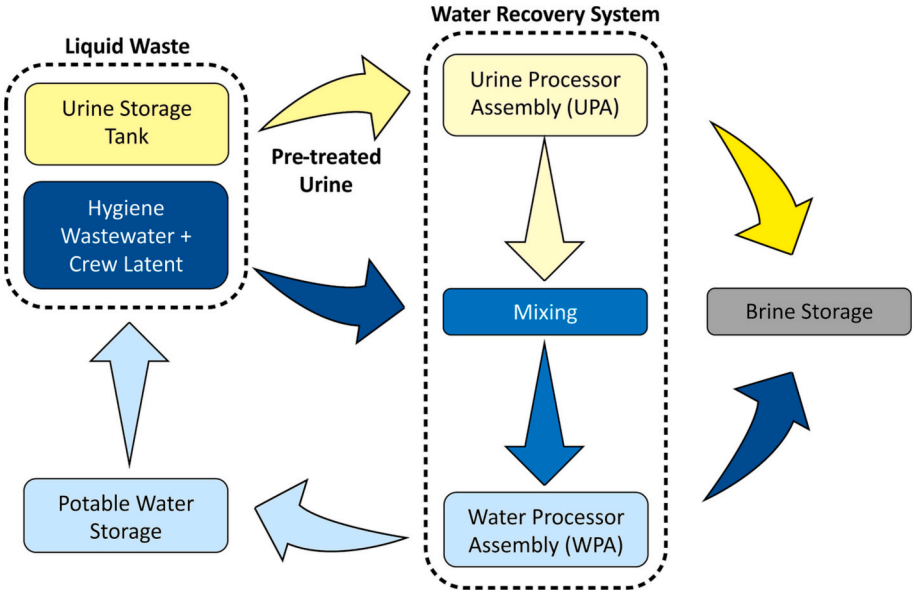

Fig. 1. Schematic diagram of the water recovery system implemented in the International Space Station (ISS), consisting of a urine processor assembly (UPA) and a water processor assembly (WPA) [14].

processor assembly (WPA), the former aimed at the recovery of water from urine, and the latter from hygiene and crews' vapor wastewater. UPA usually consists of a low-pressure rotating vapor compression evaporator. The effluent from this step is then mixed with the other wastewater sources to be purified in the WPA. The WPA block is designed to remove inorganics, non-volatile organics, and low molecular weight organics by filtration, ion exchange, and activated carbon adsorption. A final potable water product is thus obtained, while the brine of both systems is stored for discharge or to be transformed into fertilizer, a task that is currently being investigated, for example, in the "Veggie" project [7,8].

Owing to large volumes and maintenance costs of current water reuse systems, investigations on alternative components have been carried out to increase the overall recovery while lowering weight [9]. Specifically, membrane-based systems have been proposed to replace the distillation assembly in the UPA. Liu et al. [10] evaluated the performance of commercial forward osmosis membranes, which did not result in complete urea rejection. Another issue of the forward osmosis system was the high concentration polarization especially observed on the draw agent side due to microgravity and to the absence of buoyancy-driven mixing, which resulted in a substantial reduction of water flux, as determined by Flynn [11] and Chen et al. [12]. Cath et al. [13] investigated a hybrid forward osmosis-reverse osmosis system devised to reduce fouling of the RO membranes and to increase the overall rejection of pollutants. However, the removal of small compounds was found to be challenging, mainly due to the constrained use of a conventional hydrophilic polymeric membrane, as necessarily done within osmotic- and pressure-driven processes.

Membrane processes based on phase change typically show a better performance in terms of rejection of non-volatiles. Specifically, membrane distillation (MD) has high potential for space applications, as it is compact and compatible with low-grade energy sources, such as solar thermal energy [15,16]. Among different MD configurations, the simplest and most compact system is represented by direct contact membrane distillation (DCMD). The DCMD process is driven by the temperature difference between the two sides of the hydrophobic membrane, namely, the warmer feed and the colder distillate. The vapor pressure difference caused by the thermal gradient is the driving force of the process and it allows, under ideal conditions, only water vapor to pass through the hydrophobic membrane. Adequate water flux can be attained in MD, even at medium-low temperatures (40–50 °C) of the feed solution, while achieving virtually complete rejection of non-volatile contaminants. Due to the nature of its driving force, MD has been suggested as highly promising in a wide range of applications, such as brine post-treatment, produced water treatment, and crystallization [17]. MD has also been suggested in a few experimental works for water recovery from human urine. Among these, Liu et al. [10] demonstrated almost complete urea rejection under low feed temperature conditions that limit the urea thermal decomposition. Zhao et al. [18] evaluated the performance of vacuum membrane distillation for the same application, resulting in the effective removal of contaminants under optimized operating conditions.

In terms of theoretical modeling, several membrane distillation modeling frameworks have been proposed, especially for water desalination applications. The majority of previous investigations were developed assuming steady-state conditions or modeling the transient via empirical parameters calibrated from experiments. Recently, a few studies were also developed on membrane distillation by means of transient lumped-element or transient 1-D/2-D modeling. Eleiwi et al. [19] proposed a transient model for DCMD system to evaluate the time-dependent performance when the process is driven by intermittent energy sources. Karam et al. [20] developed a transient lumped-parameter model for DCMD based on conservation principles and analogy between thermal and electrical systems. Another transient model was suggested by Ali [21] to investigate the DCMD during the startup period, successfully evaluating the distillate outlet temperature. That work was then extended by Ali et al. [22] who developed a spatial transient model, thus enhancing the model accuracy and predictiveness. Most of these modeling works were system-dependent and/or based on underlying parameters often amenable to interpretation and hardly transferable to different case studies. Moreover, these models usually involved simple feed solutions with one or few salts dissolved, without considering the presence of organic and volatile molecules that can impair the distillate quality, other than productivity. Rather than specific ions, a general model should make sure of a universal parameter that describes the behavior of the solutions for the purpose of predicting the flux of both water and other components. One such universal parameter is activity.

To the best of the authors' knowledge, no modeling framework of the membrane distillation system aimed at urine reuse has been presented so far to predict the system performance under different operating conditions or to investigate the effects of operating parameters aimed at system design. To fill this gap, the purpose of this work is to evaluate the performance of DCMD for high-quality water recovery from urine wastewater. A comprehensive, transient DCMD model is proposed, and it is then validated and implemented specifically for space applications, to evaluate the separation process and to predict the final water quality. The model accounts for the activity of the mixture of salts and organics, and it carefully considers both temperature and concentration polarization phenomena, as well as the water activity changes in the mixtures by utilizing the non-empirical equation developed by Chialvo et al. [23]. Therefore, the modeling framework captures the effect on water activity for any generic solution containing both ionic and organic species, unlike previous MD modeling works that utilized specific values of the water activity obtained either by experiments or by considering only simple salts. The proposed model is thus validated by DCMD experiments performed with a synthetic feed solution mimicking urine characteristics. The effect of operating conditions on the performance of the system is then assessed by sensitivity analyses aimed at proposing rational sets of conditions in terms of temperature, cross-flow velocity, and feed pH, and to ultimately assess the potential of DCMD as a viable alternative to the current distillation assembly in the UPA section of the water reuse system.

2. Modeling and experimental methods

2.1. Model development

In membrane distillation, the driving force can be expressed as a function of the temperature and concentration differences between the liquid streams at the two sides of the hydrophobic membrane [24]. To describe the temperature and concentration profiles along the length (inlet to outlet) and height (bulk to membrane interface) of the module channel and over time, a transient 2-D continuum model was developed. During membrane distillation, heat and mass transfer across the membrane occur together and, for this reason, they should be combined. According to the literature, microgravity was found to affect the dynamics in two-phase fluids [6]. The effect of microgravity was not considered in this work; however, results are not expected to be significantly affected by this phenomenon, since only the vapor phase flow due to the partial pressure difference was considered in the membrane pores.

Specifically, a DCMD configuration, represented in Fig. 2, was modeled in counter-current mode. To mimic the operative conditions suitable in the ISS, the DCMD system was run in batch mode, i.e., the daily urine waste previously collected in a tank represents the feed solution of the system, which is recirculated into the tank during MD operation until the target recovery rate is finally reached. The recovery rate is thus based on volume and not on flow rates and it is calculated as the ratio between the collected product water from the MD system divided by the initial volume of urine liquid waste in the tank. Simulations were run up to 90–95 % recovery values to retrieve both the productivity and the product water quality. Note that the model was

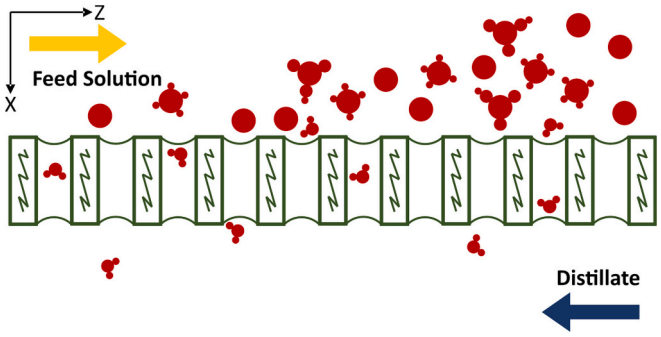

Fig. 2. Schematic diagram of direct contact membrane distillation configuration. In this work, the *z* axis refers to the feed and distillate cross-flow direction while the water flux occurs across the membrane in the *x* direction.

developed from the basic physical mechanisms occurring within the membrane channels and, as such, it has the capability of adapting to any DCMD module type and geometry other than the proposed one. The model was implemented with MATLAB software, with computation details reported in the Appendix.

2.1.1. Mass and thermal balances in the feed and distillate channels

To determine the concentration of each component as a function of space and time on the feed side, the following mass conservation equation was utilized:

$$\frac{\partial C_i}{\partial t} + \left(\vec{V}\cdot\nabla\right)C_i = D_i\nabla^2 C_i \tag{1}$$

Here, C_i is the concentration of each component, $\vec{V}$ is the velocity vector, and D_i is the molecular diffusion coefficient of the component *i*. Eq. (1) includes the mass accumulation and the convection terms on the left-hand side, and the mass diffusion on the right-hand side. For this application, it can be assumed that convection is dominant over diffusion along the channel length (high Peclet number, *Pe*). Moreover, the flow velocity in the *x* direction (over the height of the channel) can be considered negligible compared to that in the *z* direction (along the length of the channel). Based on this assumption, the equation was simplified to the following form:

$$\frac{\partial C_i}{\partial t} + u_{zf}\frac{\partial C_i}{\partial z} = D_{ix}\frac{\partial^2 C_i}{\partial x^2} \tag{2}$$

The concentration of each component at the module feed channel inlet at any time was determined by mass balance, as reported in the Appendix. To follow the feed and distillate temperature profiles as a function of space and time, energy conservation equation was considered as follows:

$$\frac{\partial T}{\partial t} + \left(\vec{V}\cdot\nabla\right)T = \frac{k_f}{\rho C_p}\nabla^2 T \tag{3}$$

Here, T represents the temperature, k_f the fluid thermal conductivity, ρ the fluid density, and C_p the fluid specific heat capacity, for both feed and distillate streams. Eq. (3) consists of energy accumulation and convection terms (left-hand side), and a conduction term (right-hand side). Similar to the mass conservation, the convection along the module length was considered dominant and the velocity in the *x* direction was neglected in the convection term, hence reducing Eq. (3) to the following form for both the feed and the distillate streams:

$$\frac{\partial T_f}{\partial t} + u_{zf}\frac{\partial T_f}{\partial z} = \frac{k_{ff}}{\rho_f C_{pf}}\frac{\partial^2 T_f}{\partial x^2} \tag{4}$$

$$\frac{\partial T_d}{\partial t} + u_{zd}\frac{\partial T_d}{\partial z} = \frac{k_{fd}}{\rho_d C_{pd}}\frac{\partial^2 T_d}{\partial x^2} \tag{5}$$

2.1.2. Heat and mass transfer across the membrane

Energy transfer through the hydrophobic membrane happens due to heat conduction and latent heat transfer [24]. To determine the temperature profile at the membrane surface along the length of module, the energy balance was modeled for both the feed and the distillate side of the membrane, as follows:

$$\frac{\partial T_{mf}}{\partial x} = \frac{1}{k_{ff}}\left(J\lambda - \frac{k_m}{d_m}\left(T_{mf} - T_{md}\right)\right) \tag{6}$$

$$\frac{\partial T_{md}}{\partial x} = \frac{1}{k_{fd}}\left(J\lambda - \frac{k_m}{d_m}\left(T_{mf} - T_{md}\right)\right) \tag{7}$$

Here, T_{mf} and T_{md} are the temperature values at the membrane surface on the feed and distillate sides, respectively, J is the water flux through the membrane, λ is the latent heat of evaporation, k_m is the membrane thermal conductivity, and d_m is the membrane thickness. These equations include both the latent heat transfer ($J\lambda$) and the conduction term $\left(\frac{k_m}{d_m}\Delta T\right)$ on the right-hand side. The vapor flux through the membrane can be expressed based on the water activity and vapor pressure differences, i.e., driving force factors [24], with the following linearized equation:

$$J = B\left(a_f P_{mf} - a_d P_{md}\right) \tag{8}$$

Here, P_{mf} and P_{md} are vapor saturation pressures on feed and distillate sides of the membrane, respectively, while a_f and a_d represent the respective water activities. Note that according to the linearized model, vapor pressures and water activity terms depend on temperature and concentration, respectively, both evolving along the module length as distillation occurs. Equations for vapor pressure and water activity are better described in Section 2.1.3. The permeability coefficient, B, was derived by linearizing the combination of the Maxwell-Stefan and the dusty-gas models, considering the interaction between the gas molecules and their collision with the pore walls [25]:

$$\frac{1}{B} = \frac{1}{\frac{\varepsilon_m P D_{wa} M}{p_a \tau R T d_m}} + \frac{1}{\frac{2\varepsilon_m r M}{3\tau R T d_m}\sqrt{\frac{8RT}{\pi M}}} \tag{9}$$

Here, ε_m is the membrane porosity, P is the total pressure, D_{wa} is the diffusion coefficient of water in air, M is the molecular weight, p_a is the arithmetic mean of the air partial pressure, τ is the tortuosity factor, R is the gas constant, d_m is the membrane thickness, and r is the membrane average pore radius. Eq. (9) includes the molecular diffusion and Knudsen diffusion resistances as the first and second terms on the right-hand side, respectively. Both resistances are effective in case $0.01 < Kn < 10$, where Kn (Knudsen number) is the ratio of the mean free path of molecules and the membrane average pore size [26]:

$$Kn = \frac{\lambda_w}{d_p} \tag{10}$$

$$\lambda_w = \frac{k_B T_m}{\sqrt{2}\pi P_m\left(2.641\times 10^{-10}\right)^2} \tag{11}$$

In the latter equations, λ_w is the mean free path of molecules, d_p is the membrane average pore size, k_B is the Boltzmann constant, T_m is the membrane average temperature, and P_m is the mean pressure in the membrane pores. The molecular diffusion resistance (first term on the right-hand side of Eq. (9)) becomes less dominant as Kn increases. As a rule of thumb, for $Kn > 10$ the molecular diffusion resistance becomes negligible (Knudsen diffusion resistance is dominant) while it becomes dominant for $Kn<0.01$ (Knudsen diffusion resistance is negligible) [26].

Based on the average pore size of the membrane used in this study (see Table 1), the value of Kn was equal to 0.65. This value implies that both resistances are effective and cannot be neglected. Therefore, Eq. (9) was utilized in the model in its integrity. In Eq. (9), the tortuosity factor

Table 1
Characteristics of the porous PTFE hydrophobic membrane used for the DCMD experiments. Data were also used as input to build the model [37].

Parameter	Symbol	Value	Unit
Thickness	d_m	77	μm
Mean pore size	d_p	0.17	μm
Porosity	ε_m	0.83	
Thermal conductivity	k_m	0.038	W $m^{-1}K^{-1}$

of the membrane can be expressed as a function of the porosity with the following equation [25]:

$$\tau = \frac{(2-\varepsilon_m)^2}{\varepsilon_m} \tag{12}$$

To quantify the temperature difference between the liquid bulk and the membrane surface over the channel height on both sides of the membrane, a temperature polarization coefficient (TPC) was considered, defined as the ratio of the space-averaged feed and distillate membrane temperature difference divided by their bulk temperature difference:

$$TPC = \frac{T_{mf} - T_{md}}{T_f - T_d} \tag{13}$$

2.1.3. Driving force terms calculation: water activity and vapor pressure

The water activity formula deployed in this study is that reported by Chialvo et al. [23] for the water activity calculation in a mixture,

$$a = 1 - \frac{1}{n_1^{\circ}}\left(\sum_{i=2}^{n+1} \upsilon_i m_i\right) \tag{14}$$

Here, υ_i and m_i are the stochiometric coefficient of electrolytes (one in case of molecular compounds) and molality of each component in the feed solution, respectively, while n_1° is the water molality. On the distillate side, the water activity is considered equal to 1, due to the assumption of almost complete rejection of contaminants and solutes. Regarding the vapor pressure, the Antoine equation was used in the following forms for water and ammonia, respectively [27],

$$log_{10}P(mmHg) = 8.05573 - \frac{1723.6425}{T\,(^{\circ}C) + 233.08} \tag{15}$$

$$log_{10}P(mmHg) = 7.58743 - \frac{1013.7815}{T\,(^{\circ}C) + 248.83} \tag{16}$$

The values of the diffusion coefficient of the various components in the solution were taken from the literature [28–32]. Moreover, properties such as fluid thermal conductivity, fluid density, fluid specific heat capacity, and latent heat of evaporation were estimated with suitable semi-empirical correlations reported in the Appendix [33–36].

2.2. Experimental setup and synthetic urine feed composition

A set of DCMD experiments was conducted to validate the model. All the tests were performed in counter-current mode, with a bench-scale system. The membrane module consisted of a 250-mm long, 50-mm wide, and 2-mm deep rectangular channel, for a total active area of 125 cm^2. The feed and distillate flow rates were maintained at 0.33 L/min during each test through calibrated flow meters (ASA, Sesto San Giovanni, Italy). The corresponding average cross flow velocity, computed considering the presence of spacers, was equal to roughly 0.068 m/s. Each test was run for 1 h to avoid any transient effects, e.g., effect of the change in feed concentration on flux. The flux across the membrane was measured by recording the change in weight of the distillate tank over time with a computer-interfaced balance characterized by a resolution of 0.05 g. On the distillate side, water with electrical conductivity below 20 μS/cm was used as distillate collecting stream. The temperature in both the feed and the distillate tank was maintained constant throughout the experiments at respective values of 55 ± 2 and 25 ± 1 °C, by means of a thermostatic water bath and a chiller, respectively. Temperature values were continuously monitored with probe thermometers directly immersed in the tanks to allow a precise setting of the thermostatic water bath and of the chiller. A PTFE membrane with the characteristics reported in Table 1 was used for all the tests [37].

The synthetic urine composition used as feed water is reported in Table 2. The different components listed in the first column were selected as representative substances to mimic a real urine sample composition from a space station, which was obtained from Thales Alenia Space (Turin, Italy). In particular, each component was chosen due to the considerable concentration in the real stream and as proxy for each family of contaminants, specifically, monovalent salts, divalent salts, dissolved organic matter, and volatiles. Urea is one of the main components of the urine mixture, and may undergo degradation during continuous operation at high temperature, thus forming ammonia species. The half-life of urea at 66 °C has been reported to be around 14 days [38,39]. Given the small active membrane area in the lab-scale system adopted in this study, experiment duration under high recovery rates would be uncharacteristically large compared with real-scale operation, and possibly result in unrepresentative urea degradation. To approach real-scale conditions, which should allow for no or negligible urea degradation, experiments were not performed by continuously concentrating the feed volume to reach a high recovery rate, but at specific conditions representing distinct recovery points, as illustrated in the following paragraph.

Each DCMD test was replicated two times and results were averaged. Tests were conducted in three main steps, as follows: (i) distilled water was initially used as feed stream to stabilize the hydrodynamic conditions and to assess the membrane permeability coefficient as well as the initial flux, without the influence of foulants and salts. (ii) The pure water feed was then replaced with the synthetic urine feed stream with the concentrations reported in Table 2, representing initial concentrations typically entering the treatment system (at 0 % water recovery factor). After flux stabilization, two samples were collected to measure the TOC and the ammonium concentration in both the feed and distillate solutions. (iii) The feed was then concentrated ten times by adding a concentrated stock solution in the feed tank, representing conditions at approximately 90 % water recovery factor, a possible final recovery value upon waste treatment. Note that to limit the ammonia formation and its diffusion to the distillate side, the feed pH was monitored continuously and maintained at 6.2 by adding small amounts of buffer agent ($NaHCO_3$) when needed. All the parameters for the simulation and the experimental tests are summarized in the Appendix; see Table A.1 of the Appendix. Moreover, the target water quality was checked against the standards imposed by the Italian legislation related to drinking water (Legislative Decree 31/2001).

Total organic carbon and ammonium contents were analyzed in the feed and distillate solutions to retrieve the observed rejection rates. TOC measurements were performed on 40 mL samples with a Shimadzu

Table 2
Synthetic urine feed composition derived from real samples. Each component was selected due to the considerable concentration in the real stream and as representative substance for each family of contaminants, namely, monovalent salts, divalent salts, dissolved organic matter, and volatiles. Data were also used as input to build the model.

Component	Chemical formula	Concentration (g/L)
Water	H_2O	
Sodium chloride	NaCl	8
Potassium chloride	KCl	1.6
Potassium sulfate	K_2SO_4	2.6
Urea	$CO(NH_2)_2$	13.5
Ammonium bicarbonate	NH_4HCO_3	0.06

(Milan, Italian branch) TOC-LCSH FA, E200 (catalytic oxidation on Pt at 680 °C), after filtration through 0.45 μm filters. Ammonium concentrations were measured with an Eco IC ion chromatography system (Metrohm, Switzerland). The conductivity in the distillate tank was measured through a conductivity meter (COND 7+, XS Instruments, Italy) during the entire duration of the tests, to detect any passage of electrically conductive solute across the membrane.

3. Results and discussion

3.1. Model and experimental results, model validation

In this section, representative results of the simulations and the respective data from the experiments are described and discussed. First, the model framework was implemented and run without any fitting parameter and under the same conditions subsequently investigated in the experimental tests. Fig. 3 reports the 2-dimensional temperature and concentration fields computed under exemplary conditions (55 °C and 25 °C inlet feed and distillate temperatures, and cross-flow velocity of 0.068 m/s) in counter-current configuration over the channel length and heights. Specifically, Fig. 3a presents simulation results for the steady-state temperature field in the MD module. On both the membrane sides, the temperature was predicted to change along the membrane length (z-dimension), mainly due to the latent heat of evaporation/condensation transported by the water vapor across the membrane and, partially, due to the heat transfer by conduction through the membrane. In fact, a portion of the feed stream energy is typically lost to the distillate stream at the expense of the process thermal efficiency. The difference between the bulk and the membrane surface temperature (x-dimension) is the result of temperature polarization, which reduces the

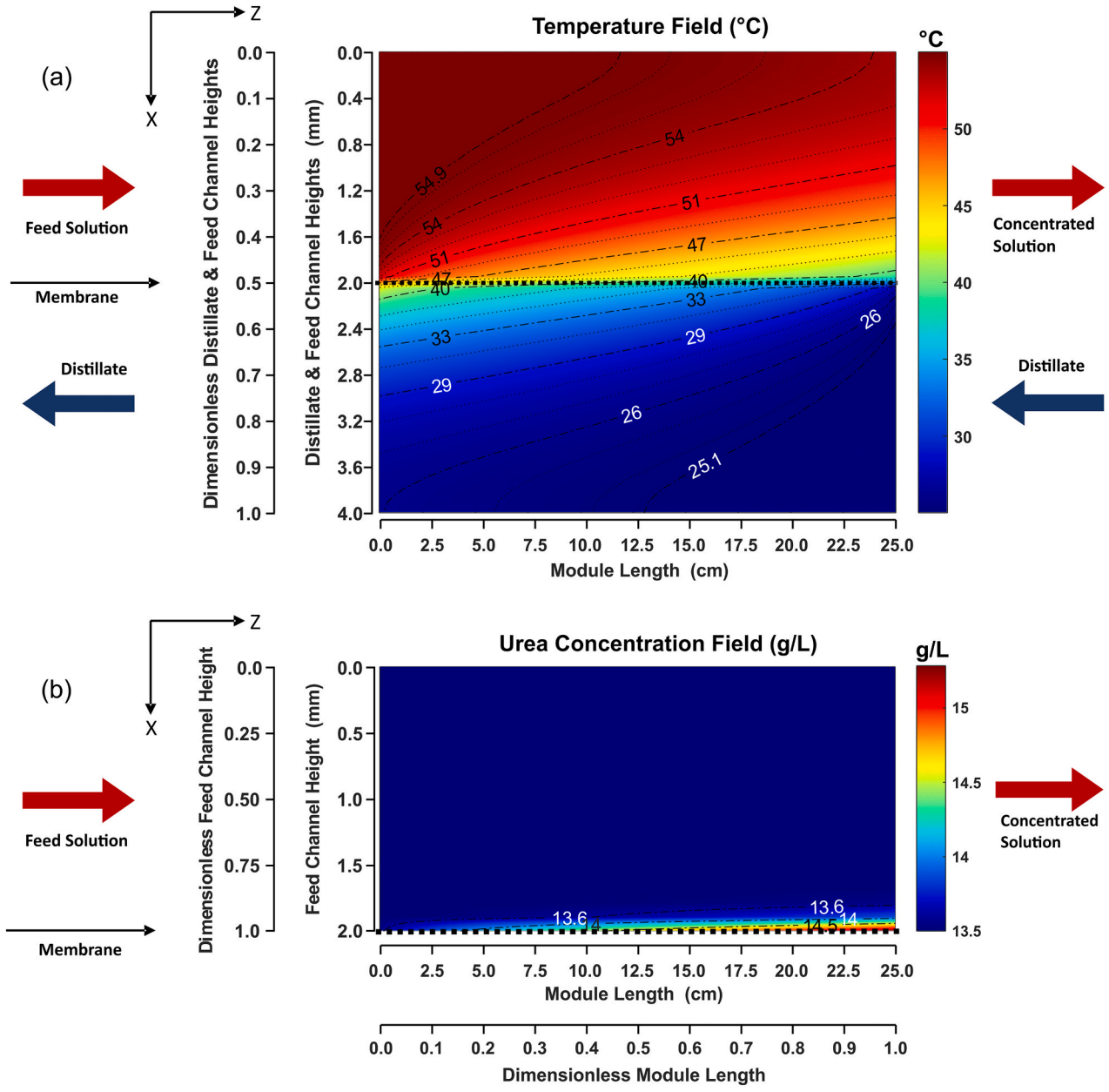

Fig. 3. Computed fields as a function of space of: (a) temperature along the feed and distillate channels at steady-state; (b) urea concentration in the feed channel, including the effect of polarizations, in the very beginning of the batch water recovery process. In these simulations, the inlet feed and distillate temperatures were set at 55 °C and 25 °C, respectively, and the two streams were characterized by the same cross-flow velocity of 0.068 m/s, that is, the same conditions used for experimental tests were simulated.

vapor pressure difference between the two sides of the membrane and lowers the transmembrane water vapor flux.

The exemplary model results for the initial concentration field of urea in the feed side of the module are depicted in Fig. 3b. The higher membrane rejection of urea compared to water translates in its increasing accumulation in the feed channel as well as near the membrane surface. Like the temperature field, the presence of a non-mixed zone close to the membrane surface increases the concentration of the rejected contaminant near the membrane surface. Concentration polarization occurs within the concentration boundary layer, which typically has a smaller thickness in comparison with the thermal boundary layer, due to the difference in the thermal and mass transfer diffusion rates. Concentration polarization increases with the vapor flux and differs for each contaminant according to their respective rejection value and their diffusion coefficient. Its value affects the water activity and contributes to lowering the transmembrane flux.

Fig. 4 shows the vapor flux computed by the model as a function of water recovery without considering any fouling or membrane wetting phenomena. Here, each orange point represents the computed water flux space-averaged across the module length. The water flux non-linearly decreases with recovery rate, starting to drop more quickly after 70 % recovery, due to faster concentration of the feed solution when its volume becomes substantially small. Specifically, for the exemplary operating conditions implemented to obtain the results graphed in Fig. 4, the model predicted the water flux to decrease from 11.4 kg $m^{-2}h^{-1}$ (at 0 % recovery) to 9.3 kg $m^{-2}h^{-1}$ (at 90 % recovery), representing approximately a 18 % loss of flux and suggesting the possibility to drive the system to even higher recovery rates while maintaining acceptable productivity.

To further validate the model, results of the simulations and of experiments were compared using water and ammonia fluxes as representative parameters. While high water flux translates into system compactness, particularly important for space applications, ammonia passage across the MD membrane may be considered as the main limiting factor for water reuse. As also presented in Fig. 4, excellent agreement was observed between the modeled and experimental water fluxes, retrieved at 0 % and 90 % recovery rate values. Additional comparisons are displayed in Fig. 5a, whereby the data predicted by the model and those observed in experiments are plotted as adjacent bars. For each considered recovery rate, modeled and experimental values were in outstanding agreement considering both water and ammonia fluxes. In quantitative terms, the maximum relative error was always below 9 % and 5 % for water and ammonia fluxes, respectively. Note that similar fluxes obtained by model implementation and experimental tests indirectly suggest that negligible flux decline occurred in the laboratory tests due to fouling. Experimental tests were not run under long-term operations to avoid any possible influence of the change in feed concentration on flux, but were sufficiently long to appreciate any possible flux decline due to fouling [40]. This result may be explained with the characteristics of the feed solution, mainly consisting of ions

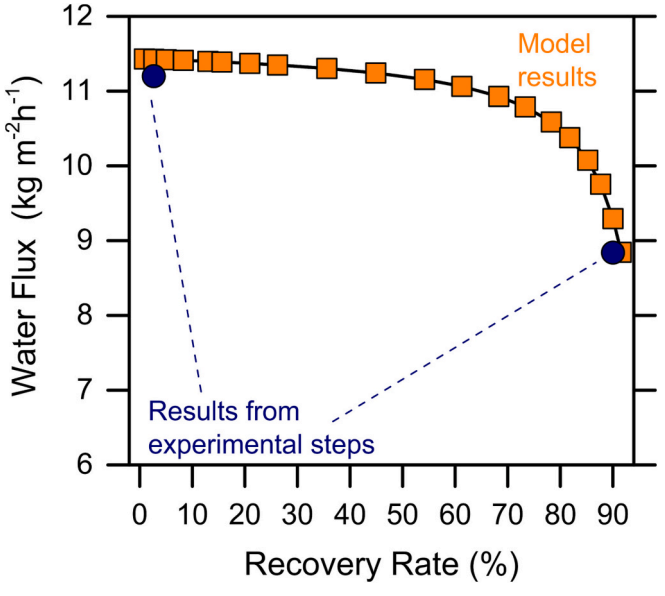

Fig. 4. Effect of recovery rate on the water flux and model validation with experimental results. Orange squares represent the modeling-based results (without any fitting parameter), while the two blue circles represent the experimental flux data obtained in two steps of the experimental test, corresponding to 0 % and 90 % recovery (each point is the average of duplicate tests). The initial feed mixture contains the components listed in Table 2; at 90 % recovery, their concentration was increased 10×. In both simulations and experiments, the inlet feed and distillate temperatures were set at 55 °C and 25 °C, respectively, and the two streams were characterized by the same cross-flow velocity of 0.068 m/s.

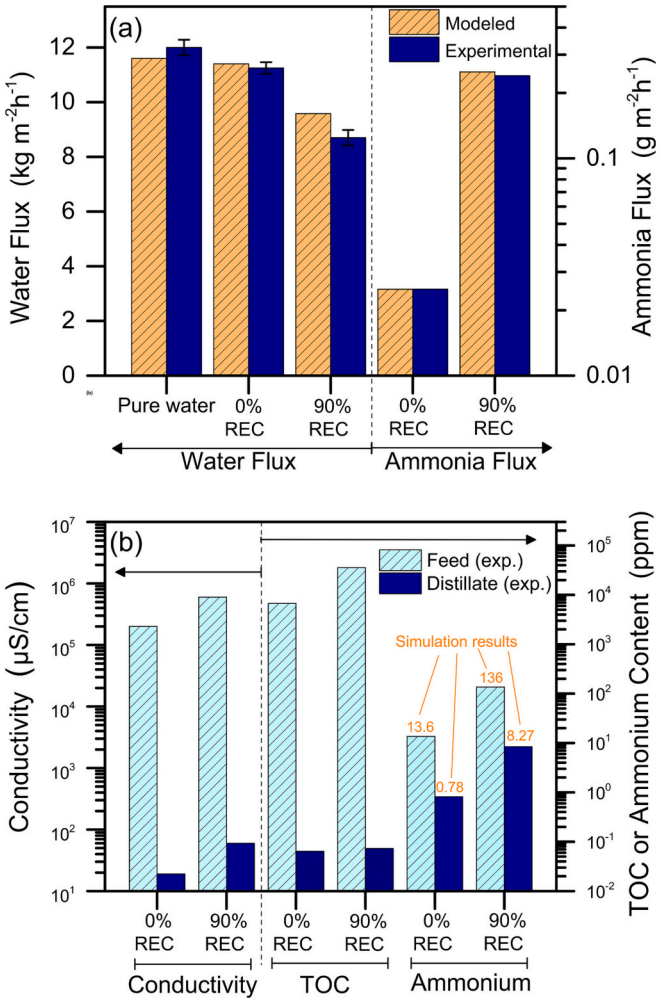

Fig. 5. (a) Modeled (orange patterned bars) and experimental (solid blue bars) results of (left axis) water and (right axis) ammonia fluxes relative to the three steps of the experimental tests, i.e., (i) initial step with deionized water as feed, (ii) the feed composition reported in Table 2, corresponding to 0 % recovery (0 % REC), and (iii) the feed composition corresponding to 90 % recovery (90 % REC). (b) Water quality results, including (left axis) conductivity, (right axis) total organic carbon, and (right axis) ammonium content of (light blue patterned) experimental feed and (dark solid blue bar) experimental distillate streams. The results of the simulations in terms of ammonium content are reported as orange labels on top of each respective bar. In both simulations and experiments, the inlet feed and distillate temperatures were set at 55 °C and 25 °C, respectively, and the two streams were characterized by the same cross-flow velocity of 0.068 m/s.

and low molecular weight solutes, the latter having a low tendency to accumulate on the membrane surface. Of course, long-term investigations should be performed in future studies to support this preliminary observation.

Overall, it can be stated that feasible water fluxes were predicted and observed, implying that this MD process may be competitive for space applications [41,42]. Specifically, considering the average daily urine production of 8 L (four crew members) in the ISS and the operating time of 10 h per day for the system, an effective membrane area of roughly 0.1 m^2 would be required based on the exemplary operating conditions discussed so far. Note that such membrane area can be achieved using a simple plate and frame module or, more advantageously, with smaller and lighter spiral-wound or hollow-fiber modules, if available [43–46]. In fact, a trade-off between simplicity and compactness exists in terms of module engineering.

In Fig. 5b, experimental results of water quality are also displayed in terms of conductivity, TOC, and ammonium ion concentration. Results validated the assumption of the high rejection of non-volatile contaminants by the hydrophobic MD membrane. Low TOC passage was observed, with values increasing from 0.064 to 0.073 ppm in the distillate while the TOC was concentrated from 6720 to 35,600 ppm in the feed tank between the two steps. The increase in distillate electrical conductivity measured at high recovery may be rationalized mainly with the ammonia passage, which partly speciates in the form of ammonium ion on the distillate side. In fact, analysis of the ammonium content revealed its presence in the distillate stream. Note that the absolute values of ammonium content predicted by the simulations (numbers above the bars in Fig. 5b) approximated well those measured in the tests, consistently with the excellent accordance in terms of ammonia flux between models and experiments. The amount of ammonium nitrogen and its volatile form, ammonia, is a critical parameter for direct reuse of the distillate stream as drinking water, and it necessitates a post-treatment step for final removal. That being said, a combination of mitigation strategies for ammonia passage may be implemented which include, for example, decreasing the feed pH of the MD step, hence moving the equilibrium conditions toward the non-volatile ionic form, and minimizing volatilization.

3.2. Temperature, driving force, and water flux distribution

Once validated, the model was utilized to determine the detailed temperature distribution within the channels, and the related space-dependent water flux values. Fig. 6a depicts the bulk and the membrane surface temperature distributions along the membrane module length, for the exemplary operating conditions discussed above and deployed in the experiments and for the exemplary initial time of the batch process, i.e., full feed tank with the urine-like composition reported in Table 2. As soon as the feed and distillate streams enter the module, the thermal boundary layers start to form and grow along the module length on both sides of the membrane, due to the incipient heat transfer. Both bulk and membrane surface temperatures varied along the axes, but with different intensities. While the bulk temperature on each side was found to change by approximately 5.5 °C from the stream inlet to the outlet, a more pronounced change of the temperature at the membrane interface was determined and was equal to 13.5 and 15.5 °C on the feed and distillate side, respectively. This variation results in an increased thermal boundary layer thickness, which in turn exacerbates the difference between the bulk and the membrane surface temperature (i.e., temperature polarization) along the module. In detail, the most important temperature variation at the membrane interface was predicted at the two extremities of the modules, resulting in roughly 10 °C difference between the two sides of the membrane surface, while 8 °C difference was observed along the central part of the module length. Note that the available driving force was found to be larger near the module extremities compared to the rest of the module, resulting in a water flux profile characterized by a minimum value around the central

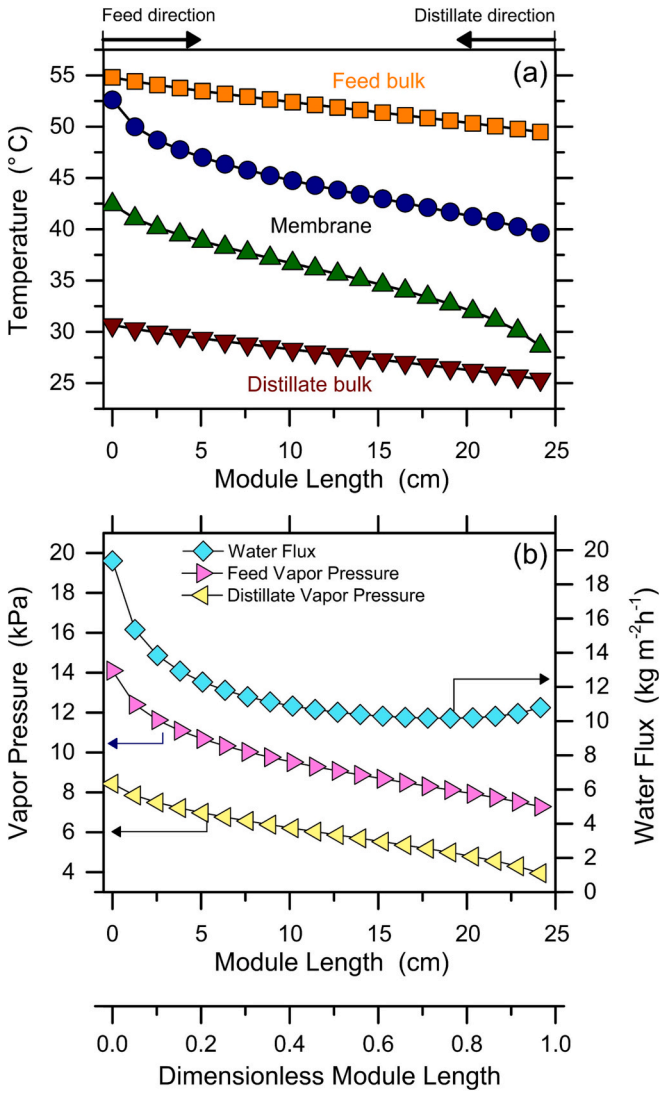

Fig. 6. Modeled results exemplified for the initial conditions of the recovery process, corresponding to a urine-like solution as feed stream (see composition in Table 2): (a) temperature distributions in the bulk solutions and at the membrane surface at both sides (feed and distillate), along the module length; (b) vapor pressure in feed and distillate channels at the membrane interfaces, as well as water flux profiles. Analogously to the results presented in Fig. 3, the temperatures of the inlet feed and distillate streams were set at 55 °C and 25 °C, respectively, while running at the same cross-flow velocity of 0.068 m/s. The same operational values were used in the experimental tests conducted to validate the model.

portion of the channel. As suggested by the temperature profiles (Fig. 6a), this phenomenon is related to the small loss of thermal energy and minor polarization effect (i) on the warm feed side at the high-temperature module end ($z = 0$) and (ii) on the cold distillate side at the low-temperature module end ($z = 1$), which offset the large polarization effects occurring on the respective, opposite side. The nearly uniform temperature difference along the module length is an advantage of the counter-current configuration, able to keep a more stable driving force and water flux distribution if compared to the co-current configuration.

The temperature difference directly influences the driving force of the MD process and ultimately the water flux through the membrane. Fig. 6b shows the resulting water vapor pressure determined in the feed and distillate stream (pink and yellow, respectively) and the ensuing water flux distribution (in light blue) when operating with the initial

feed composition in DCMD (0 % recovery, corresponding to the composition in Table 2). As expected, the vapor pressure behavior reflected closely the temperature behavior shown in Fig. 6a. However, the vapor pressure difference was found to be slightly more pronounced at the feed inlet side. This is the direct consequence of the non-linear correlation between temperature and vapor pressure, which increases the effective driving force in the points where the hot feed exerts higher temperatures. More in detail, the water vapor pressure increased by almost 5 kPa on the distillate side while it decreased by about 7 kPa in the feed from the inlet to the outlet. Consequently, the driving force difference decreased from 5.5 to 3.5 kPa from $z = 0$ (higher temperature end) to $z = 1$ (lower temperature end) along the dimensionless module length. Finally, the water flux was determined to change along the module according to the driving force difference at the membrane interfaces. While for the most part of the module length it was in the range 10–12 kg $m^{-2}h^{-1}$, it increased to roughly 19 kg $m^{-2}h^{-1}$ at the higher temperature end of the module. An implication of this distribution is that particular attention should be given to the inlet module design to avoid excessive ammonia flux as a possible side effect of an overly high productivity rate within this section.

3.3. Sensitivity analysis and system performance

3.3.1. Water productivity

The effect of inlet feed and distillate temperatures on the water flux averaged over the whole recovery process, as determined by the validated model, is presented in Fig. 7a. Overall, the flux may be increased either by increasing the feed temperature or by decreasing the distillate temperature. A minor effect on flux was found when changing the distillate temperature. This result is rationalized with the non-linear correlation between the temperature and the vapor pressure of the liquid. As an example, at 45 °C feed temperature, when lowering the distillate temperature from 30 °C to 25 °C, the average water flux was estimated to increase from 4.92 kg $m^{-2}h^{-1}$ to 6.21 kg $m^{-2}h^{-1}$ (~+25 %) while, when decreasing the distillate temperature from 20 °C to 15 °C (same step difference), the water flux was only elevated from 7.27 kg $m^{-2}h^{-1}$ to 8.08 kg $m^{-2}h^{-1}$ (~+10 %). Hence, the same nominal temperature difference between feed and distillate sides translated into different productivity values as a function of the absolute temperatures. While a feed temperature of 40 °C and a distillate one of 20 °C was estimated to result in 5.26 kg $m^{-2}h^{-1}$ average water flux, the same temperature difference when operating at 50 °C of feed (30 °C distillate), was found to produce a higher average water flux of 7.23 kg $m^{-2}h^{-1}$. See also Table 3, conditions A–C, for a summary of system performance values when changing the temperature of the two streams. Indeed, increasing the feed temperature comes at a cost in terms of energy requirements and ammonia passage.

An often-overlooked effect when operating in MD is that of the cross-flow velocity on water treatment performance. The cross-flow velocity can be tuned to decrease the boundary layer thickness and thwart both the temperature and concentration polarization phenomena. In MD, the values of the cross-flow velocity are usually lower compared to those adopted in pressure-driven membrane processes [47–49]. Such difference stems from the lower influence of osmotic pressure on water flux when operating in separation processes involving a phase change. Fig. 7b illustrates the effect of cross-flow velocity on the temperature polarization coefficient (TPC) and water flux through the membrane, both averaged over the whole recovery process between 0 % and 90 % recovery rate, as computed by the model. A cross-flow velocity range between 0.05 and 0.35 m/s was investigated to ensure a laminar flow regime. Working under laminar conditions would be of particular importance for space applications where the pumping energy consumption needs to be kept as low as possible. Results of the simulations

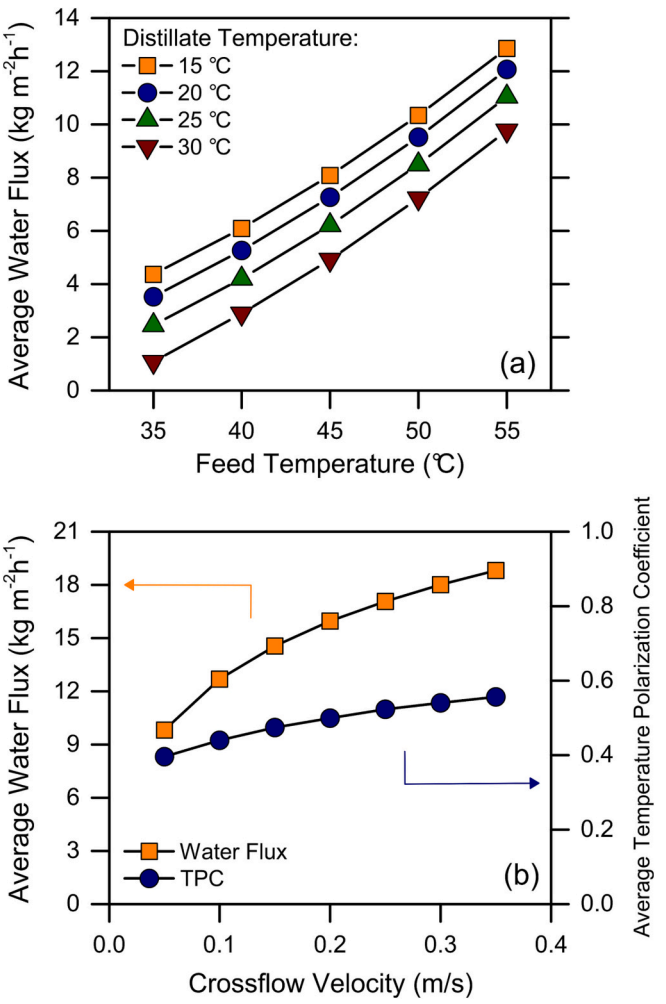

Fig. 7. Sensitivity analysis results obtained with the validated model on: (a) effect of feed and distillate inlet temperatures on average water flux (over the entire recovery process up to 90 % recovery value; initial feed composition in Table 2), when operating at a cross-flow velocity of 0.068 m/s. (b) Effect of cross-flow velocity on the average water flux and the average temperature polarization coefficient (over the entire process up to 90 % recovery). In (b), the feed and distillate temperatures were set at 55 °C and 25 °C, respectively.

imply that increasing the cross-flow velocity would elevate the TPC from 0.4 to 0.56 (Eq. (13)), thus leading to substantially reduced polarization. Not only the boundary layer is reduced when increasing the cross-flow velocity, but also the residence time of both the feed and distillate streams in their respective channels, leading to a smaller variation of the streams' temperature along the module length. As a result, the average water flux was estimated to nearly double by increasing the cross-flow velocity from 0.05 m/s to 0.35 m/s in both channels. See also Table 3, conditions B vs. D, for a summary of system performance values when changing the cross-flow of the two streams. However, further investigation should be performed to highlight the best compromise between scalability and energy requirement with the aim of minimizing costs of shipment and operation during space missions.

3.3.2. Ammonia flux and water quality

Despite the economic importance of achieving high water flux to reduce shipment and operational costs, product quality is arguably the limiting factor when the goal is direct potable reuse. The process investigated in this work is especially limited by nitrogen flux in the

Table 3
Different combinations of operating parameters of the DCMD system for urine treatment and modeled system performance.

	Operating conditions					System performance					
	Feed T (°C)	Distillate T (°C)	Cross-flow velocity (m/s)	pH	Set recovery rate (%)	Average water productivity (kg $m^{-2}h^{-1}$)	Required membrane area[a] (m^2)	Average ammonia passage[b] (g $m^{-2}h^{-1}$)	Final distillate ammonium concentration[b] (ppm)	Final distillate ammonia concentration[b and c] (ppm)	Urea chemical decomposition safe temperature zone
A	35	15	0.3	6.5	90	6.62	0.11	0.05	6.27	0.11	Yes
B	40	20	0.3	6.5	90	8.17	0.09	0.06	6.17	0.11	Yes
C	40	15	0.3	6.5	90	9.33	0.08	0.07	6.25	0.11	Yes
D	40	20	0.15	6.5	90	6.76	0.11	0.05	6.28	0.11	Yes
E	40	20	0.3	6	90	8.17	0.09	0.03	2.64	0.05	Yes
F	40	20	0.3	6.5	95	8.02	0.10	0.07	8.01	0.14	Yes
G[d]	55	25	0.068	6.2	90	11.04	0.07	>0.05	>3.7	>0.07	No

[a] System operation time is set for 10 h every day and daily urine capacity to treat is set to 8 L (4 crew members). The module length was assumed constant in all cases, to avoid any unintended change in the residence time of the stream in the module channel.
[b] The amounts for ammonia passage, as well as ammonium and ammonia final concentrations in the distillate, do not account for urea decomposition, which would increase the nitrogen content in the final water product.
[c] Distillate pH and initial volume were assumed 7.5 and 1 L, respectively.
[d] Set of conditions investigated in the experimental tests.

form of ammonia from the feed to the distillate side. Ammonia potentially derives from both the decomposition of urea and the natural presence of ammonium species in urine, which result in the formation of this harmful component when operating above certain conditions of feed temperature and pH. The modeled effect of feed solution pH on the average (between 0 % to 90 % water recovery) ammonia passage through the membrane is shown in Fig. 8. The average ammonia flux was modeled to decrease in a logarithmic way by reducing the feed solution pH. Based on the ammonia-ammonium equilibrium, reducing the pH shifts the reaction toward the production of the non-volatile ammonium species (see the equilibrium reaction in the Appendix). Conversely, at higher pH values the reaction shifts toward producing more ammonia, which is slightly more volatile than water, and may diffuse through the microporous membrane and then convert partly back to ammonium on the distillate side in accordance with the equilibrium constant. Therefore, to limit the ammonia passage and eventually ease the post-treatment steps for ammonium and ammonia removal of distillate, the pH may be lowered in a feasible range, albeit at some expense related to chemicals and system management. Interestingly, while the pKa of the equilibrium speciation is close to 9, the effect of pH change remained notable in the 5–7 pH range, when considering

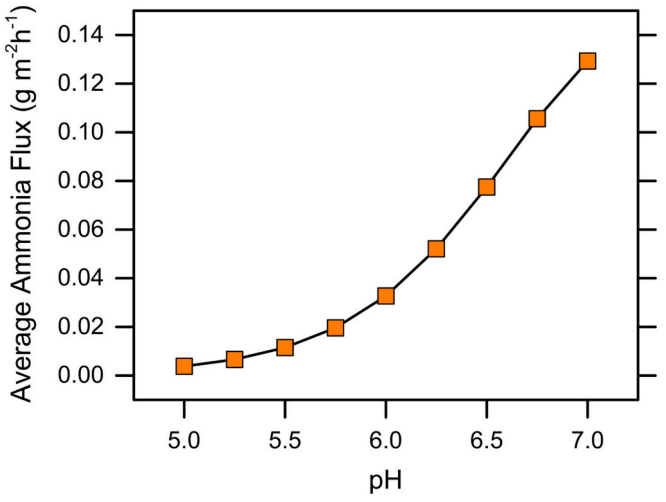

Fig. 8. Effect of feed pH on the average (between 0 and 90 % water recovery) ammonia flux obtained with the (orange squares) model. The same operational conditions were set in the model, i.e., the initial feed composition is reported in Table 2, the feed and distillate temperatures where set at 55 °C and 25 °C, respectively, and the cross-flow velocity was 0.068 m/s.

improvements in product quality: lowering the pH from 6.5 to 6 was estimated to reduce the average ammonia passage by almost 60 %, specifically, from 0.078 g $m^{-2}h^{-1}$ to 0.033 g $m^{-2}h^{-1}$. An ammonia concentration of 0.05 ppm and an ammonium concentration of 2.64 ppm were computed in the final daily distillate product when the feed pH was equal to 6 and when operating at 40 °C of feed. Also interestingly, a relevant rise in the ammonia passage was simulated when increasing the final recovery rate from 90 % to 95 %. This result highlights how the fast concentration of substances within this recovery range may impair the final water quality, hence its reuse potential. Therefore, an increase in the membrane area to further increase the recovery above 90 % would be disadvantageous for both the standpoints of system compactness and the water quality. See also Table 3, conditions B, E, F for a summary of the system performance simulated under the two pH conditions and the two recovery rates. Note that, while operating below pH 6 could potentially translate into an acceptably small ammonia flux, a post-treatment step involving, e.g., oxidation or stripping, would nonetheless be required to achieve a safe distillate quality for potable use. A multibarrier approach should be deployed to guarantee the safety of the final product and to address instances of failures or underperformance of the system.

Urea degradation to ammonia is another key factor that must be considered when choosing operating conditions. The urea in the synthetic urine feed solution utilized in the tests conducted in this work may be considered a stable compound, since the urea's decomposition half-life time in aqueous media has been reported to be in the order of years at ambient condition and of days at temperatures larger than roughly 60–70 °C [50]. In real systems, urea chemical decomposition to ammonia and carbon dioxide would be accelerated by increasing the feed temperature, e.g., in an attempt to increase system productivity. Specifically, operation under 40 °C has been recommended to be safely below temperature values that would produce substantial chemical decomposition [38]. Under such conditions, the urea half-life time of 14 days at 66 °C would ensure sufficient urea stability in the urine feed stream [38,39]. It may be argued that, within a trade-off between productivity (high temperature) and product quality (low ammonia concentration), the latter shall be prioritized, especially if the final purpose of the treatment is direct potable reuse and because this course of action would allow less cumbersome or costly post-treatment steps. Therefore, all the design conditions suggested in Table 3 are conservatively far from the urea degradation zone and would allow for a reasonable margin of safety in that respect.

That being said, the presence of urease enzyme in the human urine could drastically accelerate the enzymatic hydrolysis of urea, possibly reducing the half-life to hours [50]. Previous investigations also

revealed that the use of enzyme inhibitors could be a possible solution and two approaches have been suggested. The first strategy would be to add calcium hydroxide to increase the pH above the enzymatic hydrolysis pH range [38]. While this strategy is beneficial in terms of inhibiting urea decomposition, it results in shifting the ammonium-ammonia equilibrium reaction toward more volatile ammonia. On the other hand, it has also been reported that acidity may be exploited to inhibiting the urease enzyme [51]. This second approach would be more beneficial for this specific application, since it would accomplish two tasks: (i) reducing urea decomposition, and (ii) shifting the equilibrium toward non-volatile ammonium ions.

4. Conclusion

The DCMD process was evaluated for direct potable water reuse from urine liquid waste in space stations. A transient, 2-D model based on solution activity was developed and implemented, then experimentally validated using water and ammonia flux as representative parameters. The model results were in excellent agreement with the experimental tests performed using a synthetic urine feed. Indeed, the model was also able to predict the overall rejection of volatile ammonia as a function of recovery rate. Conductivity and TOC results confirmed the high rejection of soluble salts and organics by the DCMD system. On the other hand, non-negligible ammonia passage was observed under the investigated feed pH and temperature conditions. A sensitivity analysis was performed to observe the effect of operating parameters on water flux and on ammonia passage, respectively influencing the compactness and the final quality of the process. The influence of operating parameters such as the inlet temperatures, cross flow velocity, and feed pH were discussed, and a series of trade-offs were highlighted:

1. Increasing the cross-flow velocity within the laminar flow range resulted in substantial gains in productivity under feasible operating conditions.
2. By lowering the pH down to 5, ammonia production and passage was reduced due to the shift in the ammonium/ammonia equilibrium reaction, but the use of an acidic buffer may complicate system design and compactness.
3. In any case, the ammonia passage implies the necessity of at least one post-treatment step. The advantages or disadvantages of putting in place a system to lower the pH in the MD step (see above) shall be evaluated against those of implementing a high-performance post-treatment removal step.
4. Under the investigated combinations of operating conditions, the DCMD system was predicted to provide a productivity in the range of 6.62–9.33 $\mathrm{kg\ m^{-2}h^{-1}}$, related to a required effective membrane area between 0.11 and 0.08 $\mathrm{m^2}$ for daily (10 h operation time) urine treatment of 8 L (four crew members) in the ISS. This membrane area may be obtained either in a plate and frame module or, more advantageously, with smaller and lighter spiral-wound or hollow-fiber modules. Therefore, it would be less space consuming if compared to the current distillation assembly in the UPA, representing an advantage for space application.

Further experimental investigations should be performed using real urine, to account for the process of enzymatic hydrolysis that decomposes urea, possibly requiring feed acidification. Also, long-term and fouling phenomena should be evaluated more in detail. Overall, this study highlights that a simple, compact, and light DCMD system compatible to work with low grade energy source, such as solar thermal or waste heat recovery from electronics, might be in fact a proper alternative to the current distillation assembly implemented in the ISS.

CRediT authorship contribution statement

Ali Naeimi Tabasian: Data curation; Formal analysis; Investigation; Methodology; Validation; Visualization; Roles/Writing - original draft. **Francesco Ricceri**: Data curation; Investigation; Methodology; Visualization; Roles/Writing - original draft. **Matteo Morciano**: Methodology; Supervision; Validation; Writing - review & editing. **Giorgio Boscheri**: Conceptualization; Funding acquisition; Supervision; Writing - review & editing. **Rachele Perelli**: Conceptualization; Funding acquisition; Supervision; Writing - review & editing. **Matteo Fasano**: Conceptualization; Funding acquisition; Project administration; Software; Supervision; Writing - review & editing. **Alberto Tiraferri**: Conceptualization; Funding acquisition; Project administration; Resources; Supervision; Visualization; Writing - review & editing.

Declaration of competing interest

The authors declare the following financial interests/personal relationships which may be considered as potential competing interests: Alberto Tiraferri reports financial support was provided by Thales Alenia Space Italia.

Data availability

Data will be made available on request.

Acknowledgments

This work was funded by Thales Alenia Space and by the European Union Horizon Europe research and innovation programme under grant agreement number 101091915 (acronym “MEloDIZER”). Views and opinions expressed are however those of the author(s) only and do not necessarily reflect those of the European Union or the European Health and Digital Executive Agency (HADEA). Neither the European Union nor the granting authority can be held responsible for them.

Appendix A

A.1. Feed and distillate tanks mass balances

$$\frac{dV_{f,tank}}{dt} = -\sum_{j=1}^{n} JW\Delta z \tag{A.1}$$

$$\frac{dV_{d,tank}}{dt} = \sum_{j=1}^{n} JW\Delta z \tag{A.2}$$

A.2. Water vapor diffusion coefficient in the air [33]

$$PD_{wa} = 1.19 \times 10^{-4} T^{1.75} \tag{A.3}$$

A.3. Ammonium-ammonia reaction & equation

$$NH_4{}^+ \rightleftharpoons NH_3 + H^+ \ \mathrm{pKa} = 9.25 \tag{A.4}$$

$$\frac{NH_3}{NH_4{}^+ + NH_3} = 1 - \frac{1}{1 + 10^{(pH-9.25)}} \tag{A.5}$$

A.4. Fluid thermal conductivity coefficient [34]

$$k_f = 10^{\left(log(240+.0002S)+.434\left(2.3-\frac{343.5+.037S}{T+273.15}\right)\left(1-\frac{T+273.15}{647.3+.03S}\right)^{1/3} - 3 \right)} \tag{A.6}$$

A.5. Fluid density [36]

$$\rho_f = \left(9.999 \times 10^2 + 2.034 \times 10^{-2}\mathrm{T} - 6.162 \times 10^{-3}\mathrm{T}^2 + 2.261 \times 10^{-5}\mathrm{T}^3 - 4.657 \times 10^{-8}\mathrm{T}^4\right) + \left(8.02 \times 10^2\mathrm{S} - 2.001\mathrm{ST} + 1.677 \times 10^{-2}\mathrm{ST}^2 - 3.06 \times 10^{-5}\mathrm{ST}^3 - 1.613 \times 10^{-5}\mathrm{S}^2\mathrm{T}^2\right) \tag{A.7}$$

A.6. Fluid specific heat capacity [35]

$$C_p = 1000 \times \left(\left(5.328 - 9.76 \times 10^{-2}S + 4.04 \times 10^{-4}S^2\right) + \left(-6.913 \times 10^{-3} + 7.351 \times 10^{-4}S - 3.15 \times 10^{-6}S^2\right)T + \left(9.6 \times 10^{-6} - 1.927 \times 10^{-6}S + 8.23 \times 10^{-9}S^2\right)T^2 + \left(2.5 \times 10^{-9} + 1.666 \times 10^{-9}S - 7.125 \times 10^{-12}S^2\right)T^3\right) \tag{A.8}$$

A.7. Latent heat of evaporation [36]

$$\lambda = (1 - .001S)\left(2.5 \times 10^6 - 2.369 \times 10^3 T + 2.678 \times 10^{-1}T^2 - 8.103 \times 10^{-3}T^3 - 2.08 \times 10^{-5}T^4\right) \tag{A.9}$$

A.8. Simulation details

Backward and central finite difference were applied to the first and second order spatial differentials on uniform grids in both z and x directions, while a variable-step variable-order solver was used for time-dependent differentials. To solve the set of spatial and time-dependent differential equations, the proper initial and boundary conditions were utilized. For the channel inlet conditions, the Dirichlet condition was utilized while at the plate surface (no diffusion assumption), Neumann condition was applied for both mass and energy conservations. Furthermore, the initial inlet conditions in the channels were used for the module as well.

Table A.1
Summary of system operational parameters and conditions.

Parameter	Symbol	Value	Unit
Module length	L	250	mm
Module width	W	50	mm
Channel height	H	2	mm
Crossflow velocity	u_z	0.068	m/s
Feed inlet temperature	T_{fin}	55	°C
Permeate inlet temperature	T_{pin}	25	°C
Feed pH	pH	6.2	–

References

[1] OECD, OECD Handbook on Measuring the Space Economy, 2nd edition, 2022, https://doi.org/10.1787/8bfef437-en (Paris).

[2] S. Gormly, M. Flynn, A.S. Howe, Space cargo transport bags through membrane water treatment elements to space architecture building element: a total product sustainibility and life cycle design optimization experiment, J. Green Build. 7 (2012) 71–84, https://doi.org/10.3992/jgb.7.1.71.

[3] L.D.a.N. Harper, R. Clive, Jane Poynter, James D. Schalkwyk, Dennis Ray Wingo, Life support for a low-cost lunar settlement: no showstoppers, New Space 4 (2016) 40–49, https://doi.org/10.1089/space.2015.0029.

[4] T.Y. Cath, S. Gormly, E.G. Beaudry, M.T. Flynn, V.D. Adams, A.E. Childress, Membrane contactor processes for wastewater reclamation in space: part I. Direct osmotic concentration as pretreatment for reverse osmosis, J. Membr. Sci. 257 (2005) 85–98, https://doi.org/10.1016/j.memsci.2004.08.039.

[5] M.T. Pickett, L.B. Roberson, J.L. Calabria, T.J. Bullard, G. Turner, D.H. Yeh, Regenerative water purification for space applications: needs, challenges, and technologies towards 'closing the loop', Life Sci. Space Res. 24 (2020) 64–82, https://doi.org/10.1016/j.lssr.2019.10.002.

[6] F. Volpin, U. Badeti, C. Wang, J. Jiang, J. Vogel, S. Freguia, D. Fam, J. Cho, S. Phuntsho, H.K. Shon, Urine treatment on the international space station: current practice and novel approaches, Membranes 10 (2020) 327, https://doi.org/10.3390/membranes10110327.

[7] C. Layne, W. Jill, B. Christopher, B. Jesse, G. Daniel, S. Ryan, T. Frank, Status of ISS water management and recovery, in: Proceedings of the 45th International Conference on Environmental Systems, Washington, DC, USA, 2015. http://hdl.handle.net/2346/64360.

[8] G.D. Massa, N.F. Dufour, J.A. Carver, M.E. Hummerick, R.M. Wheeler, R. C. Morrow, T.M. Smith, VEG-01: veggie hardware validation testing on the international space station, Open Agric. 2 (2017) 33–41, https://doi.org/10.1515/opag-2017-0003.

[9] D. Muirhead, D. Carter, Dimethylsilanediol (DMSD) source assessment and mitigation on ISS: estimated contributions from personal hygiene products containing volatile methyl siloxanes (VMS), in: 48th International Conference on Environmental Systems, Albuquerque, New Mexico, USA, 2018. http://hdl.handle.net/2346/74112.

[10] Q. Liu, C. Liu, L. Zhao, W. Ma, H. Liu, J. Ma, Integrated forward osmosis-membrane distillation process for human urine treatment, Water Res. 91 (2016) 45–54, https://doi.org/10.1016/j.watres.2015.12.045.

[11] M.T. Flynn, Microgravity testing of the forward osmosis bag (FOB), a personal water purification device, in: 43rd International Conference on Environmental Systems. DOI:https://doi.org/10.2514/6.2013-3472.

[12] Y. Chen, L. Chen, H. Bai, L. Li, Graphene oxide–chitosan composite hydrogels as broad-spectrum adsorbents for water purification, J. Mater. Chem. A 1 (2013) 1992–2001, https://doi.org/10.1039/C2TA00406B.

[13] T.Y. Cath, D. Adams, A.E. Childress, Membrane contactor processes for wastewater reclamation in space: II. Combined direct osmosis, osmotic distillation, and membrane distillation for treatment of metabolic wastewater, J. Membr. Sci. 257 (2005) 111–119, https://doi.org/10.1016/j.memsci.2004.07.039.

[14] J.M. Pruitt, L. Carter, R.M. Bagdigian, M.J. Kayatin, Upgrades to the ISS Water Recovery System, 2015.

[15] M. Giagnorio, M. Morciano, W. Zhang, C. Hélix-Nielsen, M. Fasano, A. Tiraferri, Coupling of forward osmosis with desalination technologies: system-scale analysis at the water-energy nexus, Desalination 543 (2022), 116083, https://doi.org/10.1016/j.desal.2022.116083.

[16] M. Morciano, M. Fasano, L. Bergamasco, A. Albiero, M. Lo Curzio, P. Asinari, E. Chiavazzo, Sustainable freshwater production using passive membrane distillation and waste heat recovery from portable generator sets, Appl. Energy 258 (2020), 114086, https://doi.org/10.1016/j.apenergy.2019.114086.

[17] J. Lou, J. Vanneste, S.C. DeCaluwe, T.Y. Cath, N. Tilton, Computational fluid dynamics simulations of polarization phenomena in direct contact membrane distillation, J. Membr. Sci. 591 (2019), 117150, https://doi.org/10.1016/j.memsci.2019.05.074.

[18] Z.-P. Zhao, L. Xu, X. Shang, K. Chen, Water regeneration from human urine by vacuum membrane distillation and analysis of membrane fouling characteristics, Sep. Purif. Technol. 118 (2013) 369–376, https://doi.org/10.1016/j.seppur.2013.07.021.

[19] F. Eleiwi, N. Ghaffour, A.S. Alsaadi, L. Francis, T.M. Laleg-Kirati, Dynamic modeling and experimental validation for direct contact membrane distillation (DCMD) process, Desalination 384 (2016) 1–11, https://doi.org/10.1016/j.desal.2016.01.004.

[20] A.M. Karam, A.S. Alsaadi, N. Ghaffour, T.M. Laleg-Kirati, Analysis of direct contact membrane distillation based on a lumped-parameter dynamic predictive model, Desalination 402 (2017) 50–61, https://doi.org/10.1016/j.desal.2016.09.002.

[21] E. Ali, Dynamic analysis and modeling of direct contact membrane distillation for water desalination during startup using linear system theory, Chem. Eng. Process. 136 (2019) 17–27, https://doi.org/10.1016/j.cep.2018.12.003.

[22] E. Ali, J. Saleh, J. Orfi, A. Najib, Developing and validating linear dynamic models for direct contact membrane distillation during start-up over wide operating conditions, Comput. Chem. Eng. 134 (2020), 106678, https://doi.org/10.1016/j.compchemeng.2019.106678.

[23] M.R. Gennero de Chialvo, A.C. Chialvo, Prediction of the water activity in multicomponent solutions by a simple and accurate equation and derivation of Zdanovskii's rule, J. Solut. Chem. 48 (2019) 395–411. https://link.springer.com/article/10.1007/s10953-019-00869-z.

[24] E. Drioli, A. Ali, F. Macedonio, Membrane distillation: recent developments and perspectives, Desalination 356 (2015) 56–84, https://doi.org/10.1016/j.desal.2014.10.028.

[25] E. Chiavazzo, M. Morciano, F. Viglino, M. Fasano, P. Asinari, Passive solar high-yield seawater desalination by modular and low-cost distillation, Nat. Sustain. 1 (2018) 763–772, https://doi.org/10.1038/s41893-018-0186-x.

[26] X. Zhang, R. Koirala, A. Date, V. Jegatheesan, Modelling and simulation of flux prediction and salinity variation in direct contact membrane distillation for seawater desalination and brine treatment, Desalination 540 (2022), 116021, https://doi.org/10.1016/j.desal.2022.116021.

[27] C.L. Yaws, The Yaws Handbook of Vapor Pressure: Antoine Coefficients, Gulf Professional Publishing, 2015, https://doi.org/10.1016/C2014-0-03590-3.

[28] A. Siqueira, G. Chaves, J. Tanure, L. Dutra, N. Souza, T. Vianna, Determination of the diffusion coefficient in sodium chloride solution at different concentrations, J. Eng. Exact Sci. 8 (2022), https://doi.org/10.18540/jcecvl8iss3pp14053-01e (14053-14001e).

[29] J.-U. Kreft, C. Picioreanu, J.W. Wimpenny, M.C. van Loosdrecht, Individual-based modelling of biofilms, Microbiology 147 (2001) 2897–2912, https://doi.org/10.1099/00221287-147-11-2897.

[30] D.G. Leaist, J. Goldik, Diffusion and ion association in concentrated solutions of aqueous lithium, sodium, and potassium sulfates, J. Solut. Chem. 30 (2001) 103–118, https://doi.org/10.1023/A%3A1005296425604.

[31] V.M. Lobo, A.C. Ribeiro, L.M. Verissimo, Diffusion coefficients in aqueous solutions of potassium chloride at high and low concentrations, J. Mol. Liq. 78 (1998) 139–149, https://doi.org/10.1016/S0167-7322(98)00088-9.

[32] J. Winkelmann, J. Winkelmann, Diffusion coefficient of urea in water, in: Diffusion in Gases, Liquids and Electrolytes: Nonelectrolyte Liquids and Liquid Mixtures-Part 2: Liquid Mixtures, 2018, pp. 111–113, https://doi.org/10.1007/978-3-540-73735-3_364.

[33] Y. Yun, R. Ma, W. Zhang, A. Fane, J. Li, Direct contact membrane distillation mechanism for high concentration NaCl solutions, Desalination 188 (2006) 251–262, https://doi.org/10.1016/j.desal.2005.04.123.

[34] D.T. Jamieson, J.S. Tudhope, Physical properties of sea water solutions: thermal conductivity, Desalination 8 (1970) 393–401, https://doi.org/10.1016/S0011-9164(00)80240-4.

[35] K.G. Nayar, M.H. Sharqawy, L.D. Banchik, Thermophysical properties of seawater: a review and new correlations that include pressure dependence, Desalination 390 (2016) 1–24, https://doi.org/10.1016/j.desal.2016.02.024.

[36] M.H. Sharqawy, J.H. Lienhard, S.M. Zubair, Thermophysical properties of seawater: a review of existing correlations and data, Desalin. Water Treat. 16 (2010) 354–380, https://doi.org/10.5004/dwt.2010.1079.

[37] F. Ricceri, M. Giagnorio, G. Farinelli, G. Blandini, M. Minella, D. Vione, A. Tiraferri, Desalination of produced water by membrane distillation: effect of the feed components and of a pre-treatment by Fenton oxidation, Sci. Rep. 9 (2019) 14964, https://doi.org/10.1038/s41598-019-51167-z.

[38] D.G. Randall, M. Krähenbühl, I. Köpping, T.A. Larsen, K.M. Udert, A novel approach for stabilizing fresh urine by calcium hydroxide addition, Water Res. 95 (2016) 361–369, https://doi.org/10.1016/j.watres.2016.03.007.

[39] R.C. Warner, The kinetics of the hydrolysis of urea and of arginine, J. Biol. Chem. 142 (1942) 705–723, https://doi.org/10.1016/S0021-9258(18)45072-7.

[40] F. Ricceri, B. Blankert, N. Ghaffour, J.S. Vrouwenvelder, A. Tiraferri, L. Fortunato, Unraveling the role of feed temperature and cross-flow velocity on organic fouling in membrane distillation using response surface methodology, Desalination 540 (2022), 115971, https://doi.org/10.1016/j.desal.2022.115971.

[41] A. Deshmukh, C. Boo, V. Karanikola, S. Lin, A.P. Straub, T. Tong, D.M. Warsinger, M. Elimelech, Membrane distillation at the water-energy nexus: limits, opportunities, and challenges, Energy Environ. Sci. 11 (2018) 1177–1196, https://doi.org/10.1039/C8EE00291F.

[42] N. Thomas, M.O. Mavukkandy, S. Loutatidou, H.A. Arafat, Membrane distillation research & implementation: lessons from the past five decades, Sep. Purif. Technol. 189 (2017) 108–127, https://doi.org/10.1016/j.seppur.2017.07.069.

[43] G. Zaragoza, J. Andrés-Mañas, A. Ruiz-Aguirre, Commercial scale membrane distillation for solar desalination, NPJ Clean Water 1 (2018) 20, https://doi.org/10.1038/s41545-018-0020-z.

[44] F. Galiano, R. Castro-Muñoz, A. Figoli, Pervaporation, vapour permeation and membrane distillation: from membrane fabrication to application, in: MDPI, 2021, p. 162, https://doi.org/10.3390/membranes11030162.

[45] X. Yang, R. Wang, A.G. Fane, Novel designs for improving the performance of hollow fiber membrane distillation modules, J. Membr. Sci. 384 (2011) 52–62, https://doi.org/10.1016/j.memsci.2011.09.007.

[46] L. Eykens, K. De Sitter, C. Dotremont, L. Pinoy, B. Van der Bruggen, Membrane synthesis for membrane distillation: a review, Sep. Purif. Technol. 182 (2017) 36–51, https://doi.org/10.1016/j.seppur.2017.03.035.
[47] A. Hagedorn, G. Fieg, D. Winter, J. Koschikowski, A. Grabowski, T. Mann, Membrane and spacer evaluation with respect to future module design in membrane distillation, Desalination 413 (2017) 154–167, https://doi.org/10.1016/j.desal.2017.03.016.
[48] A.V. Dudchenko, M. Hardikar, R. Xin, S. Joshi, R. Wang, N. Sharma, M.S. Mauter, Impact of module design on heat transfer in membrane distillation, J. Membr. Sci. 601 (2020), 117898, https://doi.org/10.1016/j.memsci.2020.117898.
[49] R. Ullah, M. Khraisheh, R.J. Esteves, J.T. McLeskey Jr., M. AlGhouti, M. Gad-el-Hak, H.V. Tafreshi, Energy efficiency of direct contact membrane distillation, Desalination 433 (2018) 56–67, https://doi.org/10.1016/j.desal.2018.01.025.
[50] Z. Amtul, R. Siddiqui, M. Choudhary, Chemistry and mechanism of urease inhibition, Curr. Med. Chem. 9 (2002) 1323–1348, https://doi.org/10.2174/0929867023369853.
[51] H. Ray, D. Saetta, T.H. Boyer, Characterization of urea hydrolysis in fresh human urine and inhibition by chemical addition, Environ. Sci. Water Res. Technol. 4 (2018) 87–98, https://doi.org/10.1039/C7EW00271H.